A&A 395, 705–717 (2002)
DOI: 10.1051/0004-6361:20021336

Astronomy & Astrophysics

Laboratory study of annealed amorphous $MgSiO_3$ silicate using IR spectroscopy and synchrotron X-ray diffraction

S. P. Thompson[1], S. Fonti[2], C. Verrienti[2], A. Blanco[2], V. Orofino[2], and C. C. Tang[1]

[1] Daresbury Laboratory, Warrington, Cheshire WA4 4AD, Great Britain
[2] Dipartimento di Fisica, Universita di Lecce, C. P. 193 – Via Arnesano, 73100 Lecce, Italy

Received 15 May 2002 / Accepted 12 September 2002

Abstract. We present the results of combining in situ high resolution synchrotron X-ray powder diffraction and infrared spectroscopic measurements on an amorphous pyroxene powder sample annealed in the region of 1000 K. We find using both techniques that the crystalline structure formed during annealing is Mg_2SiO_4 (forsterite), but that the presence of certain features in the 10 μm band normally attributed to crystalline enstatite ($MgSiO_3$) is contradicted by spectroscopy in the 20 μm region (along with certain other 10 μm band features) and X-ray diffraction. Both indicate crystalline forsterite as the only crystalline phase formed at this temperature. We discuss the possible mechanism of forsterite formation from amorphous pyroxene and identify the presence of proto-forsteritic structures in the amorphous starting material. We suggest the likely origin of the 10 μm band "crystalline enstatite" features as being due to short-range improvements in the amorphous $MgSiO_3$ network ordering which are not necessarily accompanied by the formation of crystalline enstatite structure. These results not only suggest that the formation of crystalline enstatite dust grains via annealing may be difficult to realise at this temperature, but also highlight the possibility, in the absence of additional corroborating evidence, of misidentifying the nature of the carrier of the 10 μm "enstatite" features when observed in the spectra of objects such as comets. We also discuss the evolution of fine structure in the region of 15 to 16 μm, which may serve as an observational indicator of grain processing in stellar sources.

Key words. methods: laboratory – comets: general – stars: circumstellar matter

1. Introduction

Comets are generally assumed to have formed in the cold outer regions of the early solar nebula and therefore represent assemblages of essentially unaltered interstellar material. The current view of solar system cosmogony is of comets and planetary bodies forming together within the nebular disk encircling an already existing Sun. Within the disk, grains are thought to have accumulated first into kilometre sized cometary bodies and then into larger planetary ones (Bailey 1994). In this scheme the outer planets, at least in part, represent cometary aggregates, whilst comets themselves represent the primitive building blocks of the present-day solar system. The chemistry and mineralogy of comets observable at the present epoch ought therefore have much to tell us about conditions prevalent in the early solar nebula as they should represent repositories of the unused leftover materials from which the rest of the solar system was built.

Originally, Oort cloud comets were thought to have formed in the region between Jupiter and Neptune, approximately 5–30 AU from the Sun, and subsequently to have been scattered to the Oort cloud by gravitational interactions (Oort 1950). Later Safronov (1969, 1972) proposed that Uranus and Neptune, instead of Jupiter and Saturn, were responsible for dynamic scattering to the Oort cloud. This basic idea was confirmed later still by the detailed calculations of Fernandez & Ip (1981, 1983) and Ip and Fernandez (1988). Since it is now generally accepted that Jupiter would have scattered planetesimals largely to gravitationally unbound orbits, the majority of the present day Oort cloud comets are likely to have formed either well outside the orbit of Jupiter (e.g. Delsemme 1999), or formed at the Oort cloud distance itself (Hills 1982; Hills & Sandford 1983; Bailey 1987). Edgeworth-Kuiper belt comets on the other hand are assumed to have formed in situ and are therefore likely to have sampled even more distant, and hence even cooler, regions of the early solar nebula (out to ~45 AU, Weissman 1995).

The grains of interstellar molecular cloud dust constituting the initial material present in the pre-solar nebula have long been known to contain a significant proportion of Mg and Fe rich silicate grains typically with olivine and pyroxene compositions (Tielens & Allamandola 1990). These grains reveal themselves via characteristic infrared resonances at ~10 μm and ~20 μm and previously much work has been done on the optical characterisation of analogue amorphous silicates in the laboratory (e.g. Nuth & Donn 1982; Hecht et al. 1986; Dorschner et al. 1988; Stephens et al. 1995). The bands at ~10 μm and ~20 μm for amorphous silicates are well known to be characteristically broad and devoid of any fine structure that would otherwise be indicative of the silicate grain material

Send offprint requests to: S. P. Thompson,
e-mail: s.p.thompson@dl.ac.uk

possessing some form of structural symmetry. Given that comets formed in the cold outer regions of the early nebula where conditions would have been very close to those of the interstellar medium (Napier & Clube 1997), amorphous silicate grains can be expected to be well represented in comet mineralogical compositions. The detection therefore of fine structured features, apparently characteristic of crystalline dust, in the spectra of certain comets is thus both surprising and problematic. This is because such grains remain undetected in the interstellar medium and are generally regarded as being the product of annealing processes more characteristic of the hotter inner-nebular regions rather than the cooler outer zones. Depending on size and composition, grains from the interstellar medium are likely to survive the change from the initial cold pre-solar molecular cloud to the hotter solar nebula as far in as 1 to 3 AU from the Sun (Chick & Cassen 1997). The distance at which grains would become hot enough to crystallise is only weakly constrained as it requires detailed knowledge of the physical properties of the grain material itself.

The first piece of spectroscopic evidence suggesting the existence of crystalline silicates came in the form of a narrow sub-feature at ~11.2 μm embedded in an otherwise amorphous 10 μm silicate band. This sub-feature has been observed in several comets, including Comet Halley and Comet Hale-Bopp (e.g. Bregman et al. 1987; Campins & Ryan 1989; Crovisier et al. 1996; Russell & Lynch 1996; Hayward & Hanner 1997). Furthermore, the presence of an 11.2 μm feature in at least one dynamically young comet (Hanner et al. 1994a), along with certain laboratory evidence constraining the annealing conditions required for amorphous grains to undergo crystallisation, strongly suggests that crystallisation of the dust grains must have occurred prior to their inclusion in the comet body, as the temperatures experienced by comets during their short passage near the Sun would not be enough to promote grain crystallisation (Hallenbeck et al. 1998).

Early laboratory work on crystalline silicates (e.g. Koike et al. 1981, 1993) led to the 11.2 μm feature being widely identified by various authors with the sharp feature present in the spectrum of Mg-rich olivine. Colangeli et al. (1995, 1996) have produced fits to the 10 μm bands of several comets with ~11.2 μm features using laboratory spectra measured for different classes of crystalline silicate minerals. Observations of the Comet Hale-Bopp coma using ISO, covering the region 6–45 μm (Crovisier et al. 1997), revealed a rich variety of strong emission features attributed mainly to the presence of forsterite olivine grains (Brucato et al. 1999a). Ground based observations by Wooden et al. (1999) made when Hale-Bopp was close to perihelion have also revealed the presence of a sub-feature at ~9.3 μm which, based on the laboratory measurements of Koike et al. (1993), was attributed by them to Mg-rich pyroxene (enstatite) grains. Observations of certain Kuiper belt comets (Crovisier et al. 1999) have also shown the presence of an ~11.2 μm feature.

A link between comet dust and the dust of the debris disk surrounding the star β Pictoris was provided by Knacke et al. (1993) who compared β Pictoris observations with Comet Halley, while Greenberg & Li (1996) showed that β Pictoris dust can be modelled using porous cometary-like particles, typically 10 μm in diameter, built from aggregates of smaller sub-micron sized components. However the band-to-continuum ratio for β Pictoris was found to require the existence of a significant population of grains smaller than a few microns (Sitko et al. 1999). As these would be easily swept away by radiation pressure from the central star, they would need to be continuously replenished by the erosion of larger objects such as the Falling Evaporative Bodies identified in Herbig Ae/Be systems as in-falling star-grazing comets undergoing rapid loss of both gas and dust close to the central star (Ferlet et al. 1987; Hobbs 1986). It would appear therefore that comets are an intrinsic feature of the formation and evolution not only of our own solar system, but also of the other planetary and proto-planetary systems now being discovered. The presence of crystalline silicate dust may also reflect the early evolution of such systems. Sitko et al. (2000) have proposed that the mid-IR spectra of Herbig Ae/Be stars evolve as a function of stellar age and form a spectral sequence starting with features easily characterised by amorphous astronomical silicate, through to features consistent with processed crystalline olivine grains. Nuth et al. (2000) have suggested that the ageing of nebular dust grains, reflected in the formation of crystalline structure, could form the basis of a method for dating comets themselves since those that formed later on in the nebular history are likely to contain a higher proportion of grains with crystalline features.

In unravelling the relationship between nebular dust processing, comet formation and the evolution of the solar nebula itself it is necessary to understand how silicate materials behave when annealed in order to place constraints on the thermal histories of grains both before and after comet formation and hence on the possible conditions prevalent in the solar nebula. It has therefore become necessary to study in the laboratory the structural transformations occurring within thermally processed silicates. In particular we need to study the changes that occur as the silicate undergoes crystallisation as previous comparisons between laboratory and cometary spectra have shown cometary silicates to be best represented by laboratory spectra that fall somewhere between amorphous and fully crystalline (Hallenbeck et al. 1998). This being the case, it also raises an additional question as to what, in an astrophysical context, the term *crystalline silicate grain* actually describes.

Being directly comparable to the astronomical data, infrared spectroscopy is a suitable technique to use in the laboratory. However it is limited in the amount and type of structural information it can return about the material under investigation and for this reason we have combined this astronomically appropriate method with the high resolution structure probing capabilities of synchrotron X-ray powder diffraction (XRD). In doing so, we have obtained information on the structural evolution taking place within an annealed silicate that suggests possible constraints on the interpretation of its spectral evolution.

2. Experimental details

As a starting point in this work we have chosen an amorphous silicate manufactured so as to have the same stoichiometry as the Mg-rich pyroxene end member enstatite. We shall in time

be broadening the scope of our experiments to include other silicate compositions (including iron silicates) and will report the results of these investigations in subsequent papers. Estimates of the Mg/Si ratio for Comet Halley, obtained from the PUMA-1 mass spectrometer on board the Vega-1 spacecraft, suggest a value between ~0.5 and ~1.6 (Jessberger et al. 1988; Lawler et al. 1989). The choice of amorphous $MgSiO_3$ as a starting material is therefore broadly typical of the type of composition that may be expected in many comets.

2.1. Sample manufacture

The silicate sample used in these experiments was produced using the well known gel desiccation method (Sabatier 1950; Day 1974) according to the following prescription:

1. 0.1 M solutions of the soluble metal salts $MgCl_2$ and Na_2SiO_3 (sodium metasilicate) were mixed in the correct stoichiometric ratio to produce $MgSiO_3$.
2. The white suspension thus formed was left to settle for two days. The excess liquid was then decanted off and the remaining suspension centrifuged and washed with distilled water. This centrifuging/washing cycle was repeated three times.
3. The resulting gelatinous precipitate was then dried in air over a hot plate (100–150°C) to yield lumps of a white glassy-looking solid.

The silicate forms as a hydrated precipitate according to the reaction,

$$Na_2SiO_3 + MgCl_2 + H_2O \rightarrow MgSiO_3.xH_2O + 2NaCl + yH_2O \quad (1)$$

with the sodium salt being removed from the sample by the centrifuging/washing cycle.

To prepare the sample for presentation to both the synchrotron beam and IR spectrometer, the raw silicate was ground by hand in a mortar and pestle to give a fine-grained powder. SEM micrographs showed the particles to be typically ~100 μm with some as large as several hundreds of microns, while a limited number of particles also occupy the range from a few microns to a few tens of microns. Despite observing a substantial mass reduction during annealing, the SEM data showed no evidence of a change in particle size between processed and unprocessed samples. This method of preparation does produce particles that are rather large in comparison to the size of the cometary grains supposed to be responsible for the bands observed in the 10–20 μm spectra of such bodies (Brucato et al. 1999a). However, we think this difference is not of primary importance for the scope of the present work. Although Rietmeijer et al. (2002) have observed a size dependency in the annealing behaviour of silicate smokes, the particle sizes involved their experiments were significantly smaller than in the work discussed here. We believe therefore that the structural changes discussed in this paper are unlikely to be strongly dependent on particle size. However, we acknowledge that this point is deserving of further attention and we plan to investigate this possibility in future experiments.

2.2. Synchrotron X-ray powder diffraction

Based on the parallel beam optics of Parrish et al. (1986), the Daresbury Laboratory synchrotron radiation source (srs) station 2.3 diffractometer used in our experiment was originally constructed for ambient high-resolution powder diffraction studies (Cernik et al. 1990; Collins et al. 1992). Located 15 m tangentially from a 1.2 T dipole magnet in the 2 GeV electron storage ring (Munro 1997), it receives X-rays in the range 0.7–2.5 Å. These are filtered by a water cooled Si(111) channel-cut single crystal to give a monochromatic beam incident at the centre of the two circle (θ and 2θ) diffractometer. The sample furnace used in the diffraction experiment is mounted on the diffractometer's θ-circle with a flat-plate sample holder inside the device coincident with the centre of the θ-circle allowing Hart-Parrish diffraction geometry to be achieved (Hart & Parrish 1986). This makes the diffraction optics insensitive to changes in sample height, which is essential as small movements are inevitable when the sample is heated. The whole furnace assembly is enclosed in a stainless steel body, with incident and diffracted X-rays passing through kapton entrance and exit windows allowing measurements to be made during annealing. The diffracted beam passes through a parallel foil assembly on the 2θ arm and is detected using an enhanced dynamic range scintillation counter.

The furnace itself is based on a design by Debrenne et al. (1970), details of which are given in Tang et al. (1998). The sample crucible is made of molybdenum, chosen for its high melting point and induction characteristics, while a 1 mm deep and 15 mm diameter pressed platinum former is placed on the crucible to hold the sample and to prevent possible chemical reaction between sample and crucible at high temperatures. Heating is via a water-cooled 2 kW RF copper coil regulated by a Eurotherm 900 controller. Sample temperature is measured by a tungsten-rhenium thermocouple placed at the sample/crucible assembly. The operational temperature range is 290–2000 K with a heating response time of ~30 s. Even at high temperatures, ±1 K stability is achieved in under a few minutes. In order to ramp our sample up to the 1000 K annealing temperature, the furnace temperature was increased in steps of ~200 K over a period of approximately 5 min, with the approach to 1000 K being made in progressively smaller increments to avoid overshoot of the target temperature. Data collection began as soon as the temperature stabilised at 1000 K (approximately 2–3 min).

Normally θ–2θ XRD patterns are collected by synchronised rotation of the θ and 2θ arms. However to prevent the sample falling from the holder at high angle, the θ circle was fixed so that the sample was inclined at 10° to the horizontal incoming beam and the diffraction intensities corrected accordingly. An X-ray wavelength of 1.2995 Å (calibrated against a Si powder standard) was selected as a good compromise between peak incident flux and the requirement for low wavelength for increased X-ray reciprocal wave vector k-space sampling within the silicate. For a given X-ray wavelength, λ, this is given by

$$k = \frac{4\pi \sin\theta}{\lambda}, \quad (2)$$

where θ is the X-ray scattering angle. The significance of this relation is that the whole of the material's reciprocal space can only be sampled by the X-ray beam as the wavelength approaches zero. For srs station 2.3, the flux delivered to the diffractometer by the station's monochromator decreases significantly towards low wavelengths, thus in order to obtain good counting statistics at such short wavelengths, the integration time per point would have to be increased accordingly. This would have the additional effect of lowering further the temporal resolution of the experiment, or would have to be compensated for by reducing the angular range (which would also limit the available k-space), or by reducing the angular resolution which would reduce the k-space resolution and hence the long-range resolution in real-space (long-range oscillations in k-space correspond to short-range variations in real-space). Given these considerations and the pragmatic choice of wavelength we were able to employ scan parameters of a 2θ step size of 10 mdeg and detector integration time of 1 second per point throughout the experiment, giving a scan time of approximately 75 min for an angular range 15–60° 2θ.

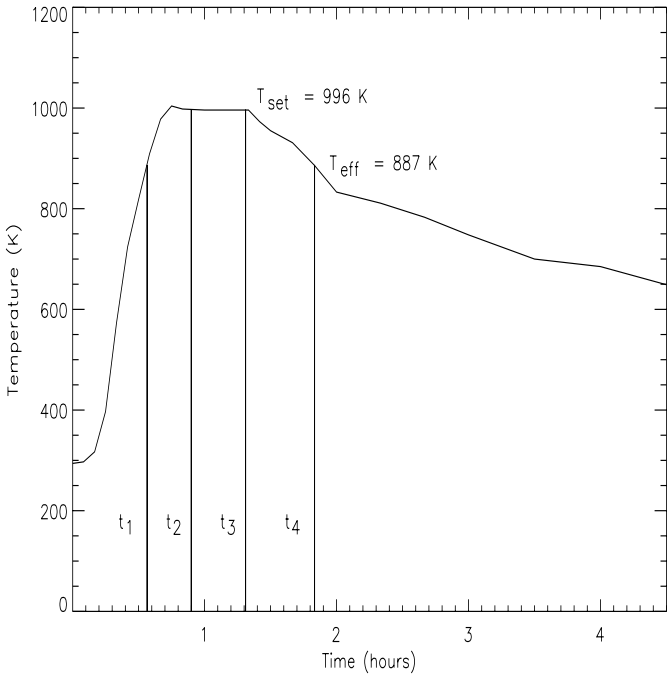

Fig. 1. Typical profile of the measured annealing temperature as a function of time for the samples used in the IR spectroscopic measurements. $T_{\rm set}$ is the nominal target temperature while $T_{\rm eff}$ is defined as 85% of $T_{\rm set}$ (in °C). Annealing begins at time $t = 0$ when the furnace is switched on. The effective temperature $T_{\rm eff}$ is reached at time $t = t_1$ and the target set point temperature $T_{\rm set}$ is reached at $t = t_2$. The furnace is switched off at $t = t_3$ and allowed to cool naturally. Finally the sample temperature crosses $T_{\rm eff}$ at $t = t_4$. The annealing time is thus defined as the time the sample has spent at or above $T_{\rm eff}$.

2.3. IR spectroscopy

In order to perform spectroscopic measurements, the samples were prepared according to the standard pellet technique as described by Borghesi et al. (1985) and Bussoletti et al. (1987). The technique is based on the dispersion of a known quantity of sample in an IR transparent matrix (KBr in our case). The resulting mixture is then compressed into a solid pellet and the sample spectrum recovered by comparison with a pellet of pure KBr.

With the obvious exclusion of the unprocessed sample, all the others were annealed in a Carbolite furnace, model CTF 12/65, capable of reaching a maximum temperature of 1200 °C. The sample compartment consists of an alumina tube approximately 700 mm in length and 75 mm in diameter, with the sample being placed at the centre of the tube on a small alumina plate. In addition to the standard furnace thermocouple we placed an additional NiCroSil/NiSil thermocouple directly in contact with the sample plate so that the annealing temperatures quoted are, to within a very close approximation, the actual temperatures experienced by each sample. During annealing, the furnace was evacuated to prevent possible reaction of the hot sample with atmospheric gases. Annealing began only when the pressure inside the furnace was less than 10^{-4} mbar. After an initial increase, the pressure remained between 2×10^{-5} and 5×10^{-5} mbar for most of the time. To further reduce the likelihood of interaction with the atmosphere, the sample was allowed to cool to ambient temperature before opening the furnace. Unfortunately the Carbolite furnace has a significant thermal inertia with no cooling system fitted. The typical annealing profile of the measured temperature at the sample plate as a function of time is shown in Fig. 1. The furnace is switched on at time $t = 0$ and switched off at time t_3 once the nominal set-point temperature, $T_{\rm set}$, has been maintained for a required period of time $\Delta t = t_3 - t_2$. As can be seen from the figure, the rise time for the temperature is relatively short (between 30 and 45 minutes) depending on the value of $T_{\rm set}$, whilst the cool-down time to ambient temperature can take more than 24 hours. The annealing times quoted in this paper therefore have been defined as the interval between the time t_1 at which the furnace reaches 85% of of the target temperature $T_{\rm set}$ (measured in °C) and the time, t_4, when the furnace subsequently cools back down to the same temperature. We are aware that such a definition may be viewed as somewhat arbitrary and that a better determination of this important parameter may be desirable. Nevertheless in the present discussion it can probably be accepted without any major disadvantage for two reasons. Firstly we have used only two basic annealing times which, in terms of the scope of the present discussion, can be simply defined as *short* (from 2 to 4 hours) and *long* (from 20 to 24 hours). Secondly the data we have obtained appears to depend quite strongly on temperature while the influence of the annealing time seems to be much weaker.

Following removal from the furnace the samples were embedded in KBr, with a pure KBr pellet also being manufactured at the same time to allow immediate subtraction of the matrix contribution to be made for spectra collected under similar conditions. The spectra themselves were recorded using a Spectrum 2000 Perkin-Elmer FT-IR spectrometer. The single beam Michelson interferometer was equipped, for the spectral range of interest (4000–400 $\rm cm^{-1}$; 2.5–25 μm), with a KBr beamsplitter, a FR-DTGS (Fast Recovery Deuterated

TriGlycine Sulphate) detector and a wire coil source at 1350 K. A resolution of 4 cm^{-1} was selected as being high enough for the convenient detection of solid state absorption features, while the measured interferograms were directly transformed in spectra using a FFT (Fast Fourier Transform) algorithm that forms part of the Spectrum for Windows software package supplied by Perkin-Elmer for operating the whole instrument.

3. Results

3.1. X-ray diffraction

Prior to annealing, the raw unprocessed silicate was scanned at room temperature using a wide-angle scan, 5–70° 2θ (Fig. 2). The background profile of this scan was used to help determine the 15–60° 2θ range of the annealing scans. Once the furnace temperature had stabilised at 1000 K it was then held constant (to within ±1 K) and the sample repeatedly scanned for 19.5 hours. During this time the diffraction data showed the evolution of a crystalline phase represented by the formation of small sharp Bragg reflections (Fig. 3) and by the end of this period a more developed crystalline diffraction pattern was clearly visible in the data, superposed upon an amorphous background that had changed little throughout the annealing period. The crystalline component had begun to form during the first scan period and by the end of the third had developed to its full extent with both crystalline and amorphous components changing little from then on. A note of caution is in order though regarding the interpretation of the development sequence shown in Fig. 3. In these diffraction scans, the XRD data is collected in angle dispersive mode, thus the 2θ axis is also a time axis within the scan (each data point being separated by the detector integration time and the unquantified time it takes the detector arm to move to, and settle at, the next point). Casual inspection of the bottom scan in Fig. 3 might suggest that high-angle structure develops before low angle structure, however this is not necessarily the case as the time difference between low and high angles means that the annealing time of the sample has increased by the time the detector reaches the high angle end of the scan. However, examination of normalised peak to continuum ratios for selected Bragg reflections supports the observation of crystallite development reaching a maximum after about the third scan: after ~5 hours, the normalised peak intensities appear constant to within the signal to noise range of the individual diffraction patterns.

Reference data from the *International Committee for Powder Diffraction Standards* (ICPDS) database allowed the crystalline phase to be identified as forsterite (Mg_2SiO_4). At this annealing temperature no Bragg reflections were unaccounted for. It is worth noting that the open olivine Mg_2SiO_4 forsterite structure would seem to be compositionally unfavourable for a sample of $MgSiO_3$. Although crystalline $MgSiO_3$ (e.g. enstatite) can be expected to yield some diffraction peaks coincident, or close to, those of forsterite, the latter accounts for all the crystalline reflections in our data. Additionally, by comparison to enstatite reference patterns, those few reflections that did occur at enstatite positions did not correspond to any of the strongest reflections expected for the enstatite structure, strongly supporting the forsterite identification.

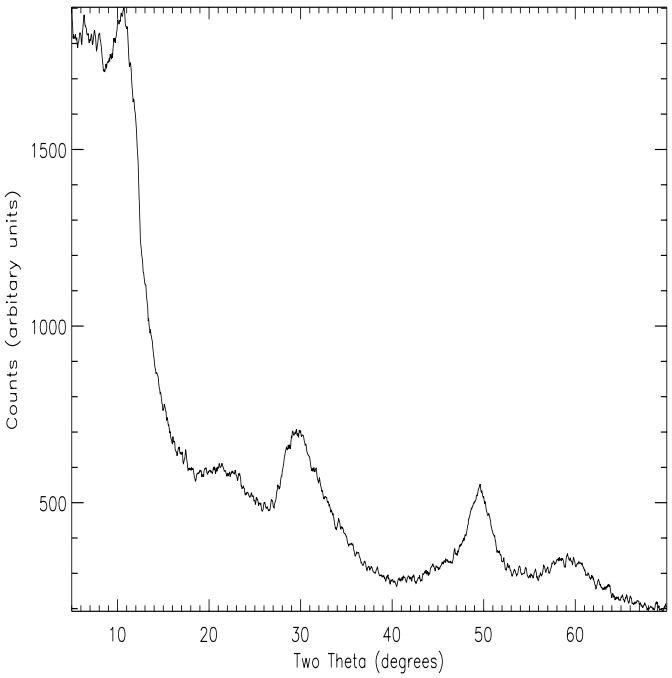

Fig. 2. XRD pattern for unprocessed amorphous $MgSiO_3$.

The asymmetric shape of the broad feature at ~30° 2θ in the raw unprocessed sample before annealing is characteristic of the presence of disordered layer-type units. If the layers were, for example, to be stacked parallel to the crystallographic 001 lattice direction, then normal crystalline reflections of the type 00*l* would be observed due to the regularity of stacking. However if the lateral displacements of the layers are totally irregular it is impossible to define lattice planes with more general Miller indices such as *hk*0 or *hkl*. So, apart from the 00*l* peaks the only other observable diffraction effects would be those originating from any 2-dimensional in-plane regularity within each separate plane. Such repeating 2-dimensional structures however would not be confined to specific Bragg angles and instead of sharp diffraction features they appear as diffuse asymmetric bands which cut off sharply on the low angle side and die away gradually on the high angle side (Whittaker 1981). These diffuse bands are characterised by two indices *hk*, and the low angle cut off is located close to the position that would otherwise be occupied by the *hk*0 reflection for the corresponding 3-dimensionally ordered structure. The powder pattern of a material comprising equally spaced parallel layers, subject to random lateral displacement, consists therefore of a single set of sharp 00*l* peaks and a set of broad asymmetric *hk* bands. The powder pattern shown in Fig. 2. recorded for our amorphous $MgSiO_3$ sample contains no sharp peaks at all, but the feature at ~30° is asymmetric and exhibits a sharp low angle rise with a gradual high angle decay. The 2θ rise begins at ~27° 2θ and gives an interlayer *d*-space of 2.7 Å, which matches the forsterite 130 layer reflection *d*-spacing. The complete absence of any normal crystalline 00*l*-like reflections is evidence that while layer-forming

forsterite components are present in our amorphous sample, initially they are not stacked parallel to each other. The feature at 60° 2θ by the same argument can be associated with the forsterite 170 inter-layer stacking distance of ∼1.35 Å, which is half the 130 d-spacing. The morphology of the diffraction pattern for the raw sample thus shows the existence of disordered proto-forsteritic units, while the presence of the other diffraction features not associated with forsteritic layering shows the co-existence of other structural units in the pre-annealed silicate. Unfortunately, simple inspection of the diffraction pattern does not allow us to make any quantitative statement regarding the relative proportions of forsteritic and non-forsteritic structures. The appearance of the pattern itself is governed by two factors. Firstly, the exponential-like decay in intensity from low to high angle is the result of scattering interference from the internal structure of the repeating molecular units, while secondly, the broad superposed features are caused by scattering interference due to the arrangement of the repeating molecular units with respect of each other (it should also be noted that it is a well known effect in amorphous diffraction that the width and intensity of features increase and decrease, respectively, as a function of increasing angle). In silicates, the dominant contribution to the measured intensity comes from the SiO_n tetrahedra. Thus the precise form of the intra-molecular "decay" curve will depend on the number of O atoms in the SiO_n units and will be some weighted sum of contributions from SiO, SiO_2, SiO_3 and SiO_4 as all such units may be expected to exist in the amorphous material. The inter-molecular diffraction features are determined by the radial distribution of the SiO_n and apart from the forsteritic layer features described above the origin of the other features can only be determined from detailed modelling, which must take into account the fact that the measured pattern represents an average of contributions from all SiO_n species and arrangements thereof. Initial modelling results indicate that apart from the proto-forsteritic layer features discussed above, none of the other features can be ascribed to specific arrangements of a given SiO_n, as each value of n tends to produce features located at similar positions to the ones in our data. However, a more detailed discussion of this will be addressed in a later publication.

Previously, Rietmeijer et al. (1986) observed annealed silicate smoke particles crystallising to forsterite and tridymite (SiO_2) rather than enstatite, which they speculatively attributed to surface energy contributions from the phases formed to the thermodynamics of crystallisation for small particles. However as already noted, the particle sizes for our sample are much larger and therefore are less likely to be susceptible to surface energy contributions. The formation of a crystalline Mg_2SiO_4 phase within a chemically well defined amorphous $MgSiO_3$ starting material, apparently contrary to expectations based on equilibrium thermodynamics, could also originate from the initial ordering of the pre-existing proto-forsteritic structure in the amorphous sample when it was first annealed. The non-appearance of unique reflections originating from other crystalline silicate phases, such as enstatite, has previously been attributed to the resistance to crystallisation of the other non-forsteritic amorphous structures (i.e. arrangements of $SiO_{n\neq4}$). This was suggested (Thompson & Tang 2001) as being due

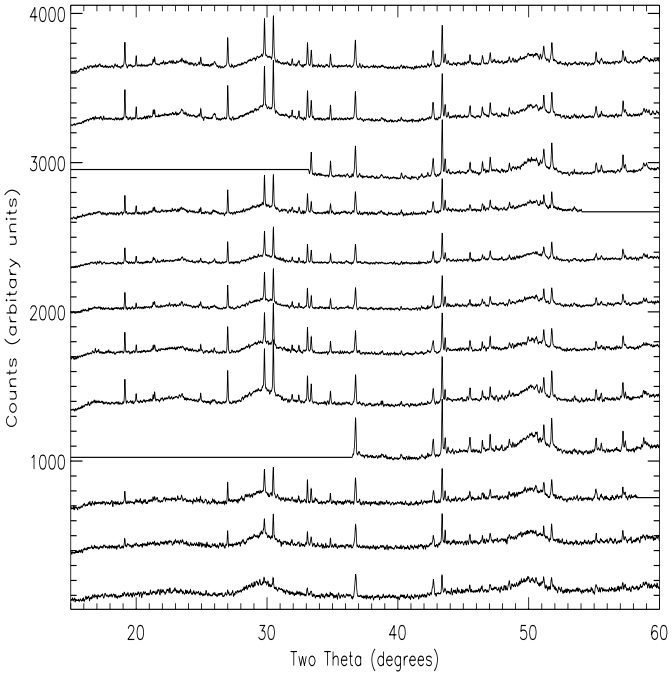

Fig. 3. XRD patterns for amorphous $MgSiO_3$ annealed at 1000 K: bottom pattern is initial exposure, top pattern after 19.5 hours annealing, middle patterns show sample data for intermediate annealing times. Straight line sections are where the synchrotron beam was unavailable due to storage ring refills. For clarity, the data in this and subsequent figures have been offset in the y-axis direction.

to the non-forsteritic amorphous arrangements being strengthened by the annealing process itself via an increase in the polymerisation of the amorphous component. One proposed mechanism by which this could occur is through annealing induced dehydrogenation of the silicate. This process could produce improvements in the amorphous silicate network connectivity and tetrahedral environment without necessarily contributing to the formation of long-range periodic (i.e. crystalline) structure. Dehydrogenation could be achieved by a recombination process such as (Shelby 1994):

$$\mathrm{SiOH + SiH \rightarrow Si{-}O{-}Si + H_2}. \quad (3)$$

This reaction is known to occur in pure amorphous SiO_2 where hydroxyl and hydride species are removed by annealing at ∼973 K or above. In the laboratory both are found to be completely removed over a period of hours (Shelby 1994). By plotting the percentage of hydroxyl/hydride removed as a function of time, the data for each species are found to fall on the same curve, implying that the effective diffusion coefficients are the same for both species. Measurement of the gas released during heating of other similar materials (Morimoto et al. 1992) confirms H_2 to be the major component along with very small amounts of water. Below ∼70% removal, the percentage removal curves approximate those expected for simple diffusion but yield an effective diffusion coefficient of $1.4{\times}10^{-7}$ cm^2 s^{-1} which is much lower than the expected value of $6{\times}10^{-6}$ cm^2 s^{-1} for simple diffusion (Shelby 1977). This experimental evidence, taken in conjunction with certain deviations of the removal curves from that of simple diffusion above 70%

removal implies that it is the reaction rate of (3) and not the diffusion coefficient that controls the outflow of molecular hydrogen from the silicate (Morimoto et al. 1992). This is further supported by the activation energy of the reaction which lies between 260 kJ mol^{-1} (Heslin 1993) and 266 kJ mol^{-1} (van der Steen 1976) and compares well with the binding energy of the SiO–H bond (264 kJ mol^{-1}, Shackelford & Masaryk 1976). It is thus the breaking of this bond that should control the dehydrogenation of the silicate. Both laboratory and cosmic silicates are likely to contain OH impurities (Steel & Duley 1987; Timmermann & Larson 1993), while SiH impurities are also likely to form in silicates produced in H-rich environments (Blanco et al. 1999). The investigation of the dehydrogenation mechanism as a process for polymerisation during annealing is currently the subject of ongoing experiments.

The net effect, however, of a process such as (3) in the annealed $MgSiO_3$ silicate would be to increase the overall polymerisation of the amorphous network by reconnecting inter-tetrahedral Si-O-Si bridging bonds and thus raise the average number of bridging oxygen atoms per tetrahedral unit (i.e. decrease the non-bridging oxygen number per tetrahedron, NBO/T). Since the amorphous silicate will initially have a distribution of NBO/T values, annealing will at first promote the ordering of $NBO/T = 4$ species only and crystal growth stalls when the need for more $NBO/T = 4$ units can only be met by breaking bonds for units with $NBO/T \leq 3$. Annealing induced polymerisation would have meanwhile reduced the bulk NBO/T for these species down towards that of SiO_2 (i.e. $NBO/T \rightarrow 0$). The mixed amorphous/crystalline state would thus persist until enough energy has been input to the system to allow the increased number of multiple bridging bonds to be broken, whereupon the amorphous phase breaks down and further crystal growth becomes possible.

3.2. IR spectroscopy

Initially, for parity with the XRD measurements, IR data were collected for the raw sample and an annealing temperature of 1000 K for short and long exposure times (2 and 20 hours respectively). However the results for the annealed sample showed the formation of considerable fine structure in both the 10 μm and 20 μm regions for both annealing times. The lack of temporal discrimination in spectral development at this temperature relative to the XRD data is likely due to differences in the annealing profile of the IR method, where annealing must be done off-line, compared to that of the on-line furnace used for the diffraction measurements. Thus in order to separate out the effects of the annealing time from those of the annealing temperature we performed a series of measurements at several lower temperatures leading up to 1000 K. With the exception of the 1000 K data and one intermediate temperature, data were collected for annealing times of 4 and 24 hours. The results of these measurements are shown in Fig. 4.

The normalization of the measured spectra was done without taking into account the actual mass of the samples examined as such a procedure would have been unreliable for two reasons: firstly, the exact determination of the mass of the sample dispersed into the KBr was rather difficult due to the limited amount of raw material available; secondly, there were certain associated difficulties in evaluating the precise effect of the substantial mass reduction that occurred during the annealing process. In order to compare the spectra in a meaningful way, we set to zero the lowest point of each absorption spectrum in the range 8–24 μm, by subtracting from each an appropriate value. We then set to 1 the highest value in the same range, by multiplying each spectrum by the appropriate scaling factor. The range 8–24 μm was selected as being the more significant for the purpose of the present paper since it is the range where silicates, in addition to their main features, also exhibit an absorption minimum. Even if normalising all the spectra to the interval 0 to 1 by this somewhat arbitary method means we can not make a quantitative comparison between the different spectral features, it does at least allow for an easy comparison to be made of the various spectral modifications induced by the annealing process.

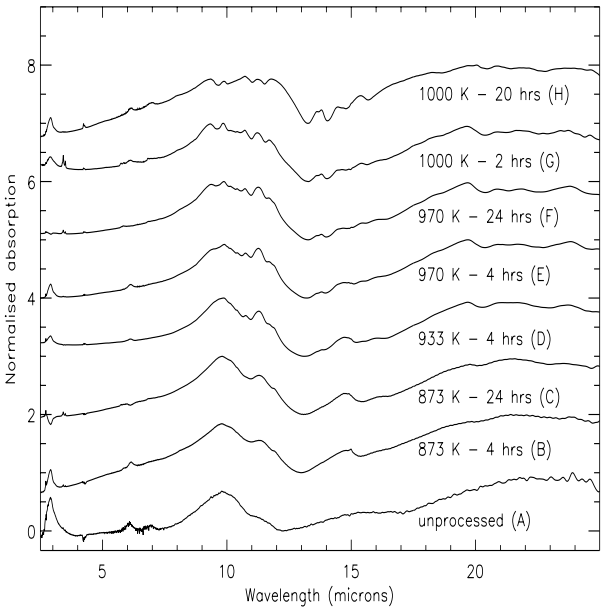

Fig. 4. Normalised IR absorption spectra for $MgSiO_3$ annealed over the temperature range 873 K to 1000 K for *short* and *long* annealing times.

3.2.1. Evolution of 10 μm and 20 μm bands

The evolution of fine structure is clearly visible in both regions over the entire time/temperature range (see Fig. 4). The development of features in each of the bands occurs as follows (see also Figs. 5 and 6).

Unprocessed sample: the 10 μm region consists of a single broad band with a peak at 9.8 and a shoulder at ~11.2, while the 20 μm region consists of a single broad band peaking at ~22.0 μm.

873 K annealed for 4 hours: the 10 μm band still peaks at 9.8 μm, but the shoulder at 11.2 μm has now developed into a peak at ~11.3 μm. There is an additional weak shoulder

feature discernible at ~11.8 μm. The 20 μm region now contains three broad features at ~19.7, 21.5 and 23.7 μm.

873 K annealed for 24 hours: the 10 μm band appears similar to the previous 4 hour data set, while the definition of each of the three 20 μm band features present in the 4 hour sample has improved.

933 K annealed for 4 hours: the 9.8 μm peak appears slightly asymmetric on its low wavelength side, a new feature at ~10.7 μm has appeared and the 11.2 μm feature possesses a weak shoulder at ~11.7 μm. The three features in the 20 μm region appear stronger than before and the middle one at ~21.5 μm has flattened and shows evidence of beginning to split into two sub-features.

970 K annealed for 4 hours: the asymmetry of the 9.8 μm peak has evolved into a shoulder at ~9.4 μm, while a weak feature at ~10.4 μm has appeared in addition to the other previous features at 10.7 and 11.2 μm. The shoulder feature at ~11.7 μm has developed further. In the 20 μm band, four distinct features are now present at 19.7, 20.9, 21.6 and 23.8 μm. The middle two having evolved from the splitting of the flattened 21.5 μm feature seen in the previous spectrum.

970 K annealed for 24 hours: the previous shoulder at 9.4 μm is now a discernible feature, while a further very weak feature has appeared at ~10.1 μm. The weak feature at 10.4 μm that first appeared in the previous data set has developed slightly while features at 10.7, 11.2 and 11.67 μm are now well established. In the 20 μm region no new features have formed, but the existing four have improved in definition.

1000 K annealed for 2 hours: well developed features are found at 9.3, 9.8, 10.7, 11.2 and 11.7 μm along with the two very weak features at 10.1 and 10.4 μm. The 20 μm band has undergone further development and now shows weak peak features at 19.6, 20.8, 21.7, 22.7, 23.4, 23.7 and 24.5 μm, with possible weak shoulders at ~24.1 and 22.0 μm.

1000 K annealed for 20 hours: the 10 μm band shows five distinct features at 9.3, 9.8, 10.73, 11.24 and 11.79 μm. The weak features at 10.1 and 10.4 μm discernible in the previous data sets being no longer visible. The five main features of the 20 μm region show evidence of further fine structure modulation, with peaks at 18.2 μm (plus a very weak feature at 18.52 μm), the feature at 19.6 μm in the previous data set now appears split into two features at 19.7 and 20.0 μm. There is a feature at 20.8 μm and a broad feature centred at ~21.9 μm which shows evidence of splitting into three very weak features, as does the one centred at ~23.7 μm. The feature present at 24.6 μm in the previous 2 hour spectrum is also present in this spectrum. Overall, these additional fine structure modulations are very small compared to the main features themselves.

3.2.2. Evolution of the 15 μm region

Although this paper is primarily concerned with the evolution of the 10 μm and 20 μm bands, we note that several features in the region of 15 μm also evolve as a function of annealing (Figs. 4 and 7). Comparison to the behaviour of the features at 10 μm and 20 μm suggests the 15 μm band features are related to, or follow, the 10 μm band features. Like the 10 μm band their development also appears to depend largely on annealing temperature.

Unprocessed sample: the 15 μm region comprises a single broad hump stretching between ~12.2 and 17 μm, peaking at ~15 μm.

873 K: an asymmetric feature has developed at ~14.8 μm, along with a weak broad feature at ~16.1 μm. This last feature appears slightly stronger with longer annealing time.

933 K: an additional weak feature has formed at ~15.4 μm with a weak double feature at ~13.7 μm also being apparent.

970 K: the ~15.4 μm feature and ~13.7 μm double feature strengthen slightly, but appear similar to the 933 K spectrum and do not evolve with annealing time.

1000 K: the ~13.7 μm double feature has now increased in strength, as has the ~15.4 μm feature. The ~14.8 μm feature shows signs of fine structure, while the ~16.1 μm feature appears to weaken, disappearing altogether from the 20 hour spectrum. At this temperature the remaining features appear to strengthen with annealing time.

Similar features are present in certain of the crystalline silicate spectra published by Jäger et al. (1998) for forsterite and pyroxene compositions and are most likely to be due to overtone resonances of the Si-O stretch vibrations responsible for the 10 μm band features. The ~14.8 μm feature in forsterite is attributed by them to a SiO_4 symmetric stretch overtone. However this feature is also present in their pyroxene data. The ~16.1 μm feature corresponds to a SiO_4 asymmetric bend and is absent from their pyroxene data. The ~13.7 μm double feature could possibly correspond to the symmetric stretch overtones at 13.6 and 13.8 μm in the Jäger et al. data, albeit shifted. Again, however, this feature is also present in their pyroxene data. Finally, the ~15.4 μm feature is present only in Jäger et al.'s pyroxene data, but with no assignment. Thus the features in this band do not appear to be diagnostic of crystalline type. On the other hand, these features do appear to represent a clear diagnostic of intermediate annealing and should be searched for in stellar spectra as an indicator of thermal grain processing.

4. Discussion

Features appearing in the 10 μm band can be associated directly with changes in the Si-O bonding state and in particular with SiO_n structural units. It is partly for this reason that both laboratory investigators and astronomers have tended to concentrate on the analysis of the 10 μm band. However, as this paper compares spectral evolution with long-range structural evolution, it will prove instructive in the present instance to consider the evolution of the 20 μm band first.

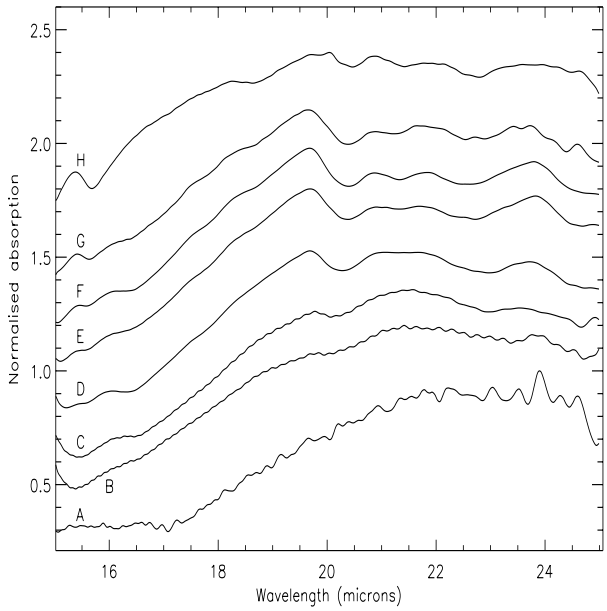

Fig. 5. Normalised IR absorption spectra for 20 μm band of $MgSiO_3$ annealed over the temperature range 873 K to 1000 K for *short* and *long* annealing times: (A) unprocessed sample, (B) 873 K for 4 hours, (C) 873 K for 24 hours, (D) 933 K for 4 hours, (E) 970 K for 4 hours, (F) 970 K for 24 hours, (G) 1000 K for 2 hours and (H) 1000 K for 20 hours.

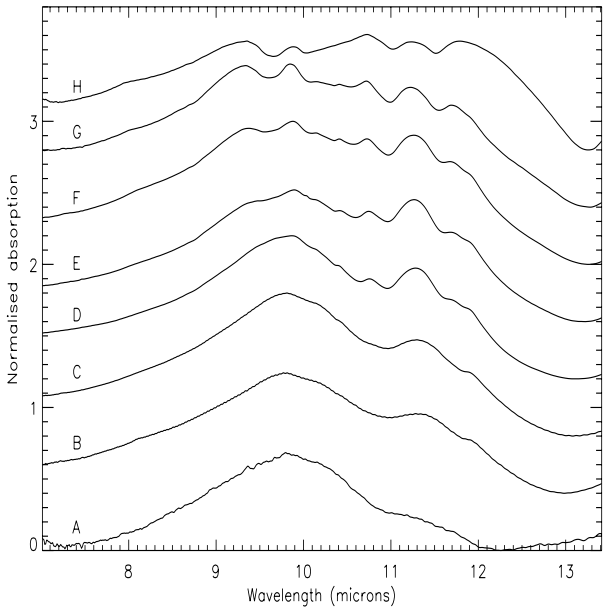

Fig. 6. Normalised IR absorption spectra for 10 μm band of $MgSiO_3$ annealed over the temperature range 873 K to 1000 K for *short* and *long* annealing times: (A) unprocessed sample, (B) 873 K for 4 hours, (C) 873 K for 24 hours, (D) 933 K for 4 hours, (E) 970 K for 4 hours, (F) 970 K for 24 hours, (G) 1000 K for 2 hours and (H) 1000 K for 20 hours.

4.1. Structural change and the 20 μm band

Annealing for 4 hours at 873 K produced three broad 20 μm band features which became more pronounced by 933 K, splitting into four features at 970 K with numerous minor additional fine-structure features appearing at 1000 K. At each of the lower temperatures the IR features appear to be insensitive to annealing time, with spectra showing little variation between the short and long annealing periods used in the experiment.

Originating generally in the vibrational modes associated with the inter-tetrahedral bend, changes in the morphology of this band are accepted as markers for changes occurring in the longer-range silicate network arrangement (Nuth & Hecht 1990). Although no direct correlation exists between the specific spectral components in this band and any physical parameters specifically related to the longer-range structure of silicates, such as the number of inter-linked tetrahedra etc. (McMillan 1984a, 1984b), the formation of fine structure in this band can be taken as indicating that the overall silicate structure does indeed evolve as a function of annealing temperature. With the exception of the 11.2 μm feature, the 20 μm band features appeared to form earlier than those at 10 μm and had quickly stabilised during the shorter annealing times. This behaviour mirrors that seen in the XRD data, which showed long-range crystal growth stabilising over a similar time scale and did not appear to evolve further with annealing time.

Jäger et al. (1998) have published peak positions for several Mg-rich crystalline olivine (forsterite) and pyroxene (clino- and ortho-enstatite) minerals (taken from transmission measurements without background correction). For the three 20 μm band features seen in our 933 K spectra, where they are most developed, at 19.7, 21.5 and 23.7 μm, the Mg-rich pyroxene data of Jäger et al. lists peaks at 19.3, 21.6 and 23.2 μm while their synthetic forsterite data shows peaks at 19.5, 21.5 and 23.5 μm. Overall the three peaks in our 20 μm band data appear to be represented quite well by Jäger et al.'s Mg-rich forsterite figures. Considering now our 970 K spectra, the four features peak at 19.7, 20.9, 21.6 and 23.8 μm, compared to the Jäger et al. pyroxene values of 19.3, 20.6, 21.6 and 23.2 μm and synthetic forsterite values 19.5, 20.8, 21.5 and 23.5 μm. Again our data is best represented by forsterite. The assignment of these features to forsteritic olivine matches the identification of the crystallite by the XRD analysis. Interestingly, Jäger et al. attribute the forsterite vibrations at 19.5 μm to the symmetric inter-tetrahedral bend, the 20.8 and 21.5 μm features to SiO_4 rotation and their 23.5 μm feature to the translational vibration of a Me^{2+} metal ion. This last feature is the one that appears to differ most between their pyroxene and olivine samples. Jäger et al. note it as being stronger in olivine than pyroxene as well as located at different wavelengths for different Fe content and mineral type. In our data this feature appears to be the 20 μm band feature to develop first in both strength and narrowness. It is likely that the ionic translational freedom will be strongly influenced by its local molecular co-ordination and hence the feature will strongly reflect the surrounding crystal symmetry. The presence of this feature, in combination with the 11.2 μm feature (see below), is likely therefore to be a strong diagnostic for the presence of a forsteritic structure.

4.2. Structural change and the 10 μm band

Unprocessed, our sample showed a shoulder at ~11.2 μm which formed a feature after 4 hours annealing at 873 K. At this

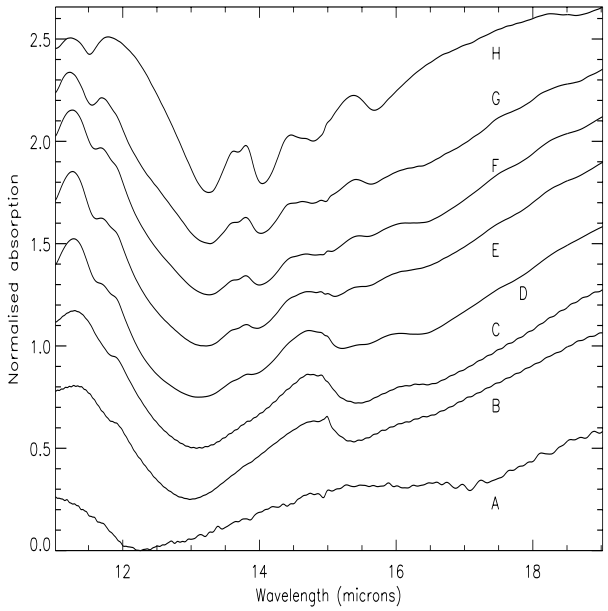

Fig. 7. Normalised IR absorption spectra for 15 μm region of $MgSiO_3$ annealed over the temperature range 873 K to 1000 K for *short* and *long* annealing times: (A) unprocessed sample, (B) 873 K for 4 hours, (C) 873 K for 24 hours, (D) 933 K for 4 hours, (E) 970 K for 4 hours, (F) 970 K for 24 hours, (G) 1000 K for 2 hours and (H) 1000 K for 20 hours.

temperature the overall 10 μm band morphology had changed little with respect to the unprocessed sample. At 933 K further features and shoulders formed, continuing to grow at 970 K and 1000 K. Overall this band appeared more sensitive to annealing than the 20 μm band. It has long been known that spectral components within this band can be identified which correlate directly with tetrahedral species with differing numbers of *NBO* atoms (Nuth & Hecht 1990) and can in principle be used to determine the relative proportions of network, sheet, chain, dimer and independent tetrahedral units present in the silicate (Thompson 1996). Features within the 10 μm band originate in the Si-O fundamental stretch mode which is strongly influenced by whether the oxygen is a bridging or non-bridging atom. Lack of variation of the 10 μm band peak intensity and shape relative to the 20 μm band in amorphous systems, has previously been taken as evidence that the features within the 10 μm band are insensitive to the longer-range structure of the silicate (McMillan 1984a, 1984b). The fact that our data shows band features that vary with both time and temperature suggests that during annealing the short-range local tetrahedral environment evolves without necessarily impinging on the longer-range inter-tetrahedral network structure. At present we are unable to comment on whether the changes in the 10 μm band are precursors to eventual change in the 20 μm band or whether the 10 μm band evolution represents the short-range environment adapting to the imposition of long-range structure.

The stability of both the 20 μm band features and long-range XRD data suggests that any physical changes associated with variations observed in the 10 μm band do not impinge on the silicate network structure, although this last statement needs some qualification. From the XRD measurements we can determine two limiting lengths. The first is the smallest real-space separation we are able to resolve using X-rays. For any angle dispersive diffraction experiment performed at a given X-ray wavelength the k-space maximum is determined by the maximum scattering angle, $\theta_{\max}$, and in turn corresponds to a minimum real-space distance below which we can not probe,

$$d_{\min} = \frac{\lambda}{2 \sin \theta_{\max}}. \quad (4)$$

For the maximum scattering angle of 30° used in this work this gives $d_{\min} = \lambda = 1.2995$ Å. The second limiting length is the length over which the regular crystalline structural arrangements are correlated. The latter can be estimated from the full width at half maximum ($FWHM$) of the crystalline Bragg reflections using the well known Scherrer equation (e.g. Warren 1969),

$$D = \frac{0.94\lambda}{B(2\theta)\cos\theta}. \quad (5)$$

This expression relates the crystallite size, D, to the $FWHM$ of a 2θ reflection ($B(2\theta)$, in radians) at the reflection's Bragg angle, θ. Although originally derived for cubic systems, the Scherrer equation is widely used for non-cubic systems and gives a good estimate value for the crystallite size if D is interpreted as the average crystal dimension in the direction perpendicular to the reflecting lattice planes. This distance therefore represents the correlation length over which the lattice separations responsible for producing the reflection are maintained. The crystallite sizes for those peaks due to layer reflections, such as the 130 peak give consistent sizes of ~0.15 μm, while for 3-dimensional lattice planes we find ~0.10 μm. For the 130 d-space of 2.7 Å, this suggests that ordering extends over ~555 layers.

Within the experimental noise inherent in the counting statistics the crystallite appears to show no systematic growth with annealing time, although the diffraction peak intensities, when corrected for synchrotron beam decay do show an initial increase with annealing time for the first few scans, which we interpret as being due to the initial formation of crystalline structure (possibly localised). The lack of subsequent growth can be interpreted in several ways, either as a stall in the physical extent of crystalline development within the sample particles (since the reflection widths show no systematic decrease with annealing time, suggesting the number of participating layers is constant), or a stall in the total number of crystallites (since the peak intensities do not increase). This latter could be due either to the number of crystallite nucleation centres being fixed during sample manufacture, with no new centres forming during annealing, or to the physical properties of the sample particles. In preparing our sample for presentation to the synchrotron beam, the particle size distribution was not tightly constrained. The sample powder was ground by hand in a pestle and mortar, which does not produce a monotonic grain size distribution (as evidenced by SEM). From our present data we are unable to address the question as to what extent the thermodynamic contribution of particle surface area affects the crystallisation process. It is also difficult to tell from either the XRD or SEM data whether the crystallite size, D, represents

a whole particle size (in which case only the smallest particles would appear to have crystallised), or whether it represents either the size of crystalline "inclusions" within otherwise amorphous particles, or a crystallite domain size within fully crystallised particles. If D does represent the whole crystalline particle size, we would have expected a systematic increase in its value with integrated annealing time as grinding of the sample produced a range of grain sizes which we would expect to have successively succumbed to crystallisation as annealing progressed. Furthermore, the overall initial change in the amorphous component of the diffraction patterns at 1000 K (e.g. narrowing of the diffuse diffraction features relative to those in the unprocessed sample) clearly indicates that structural change does occur throughout all our sample (remember X-ray diffraction represents an average snapshot of the bulk whole-sample structure). Since crystallisation only occurs in an amorphous material at the expense of its amorphousness, it is unlikely that such apparent changes would be confined to only the very smallest particles and still show up in the diffraction patterns. Additionally, Hallenbeck et al. (1998) interpreted the formation of an Si-O stretching band morphology with well defined features near 9.8 μm and 11.2 μm as a natural consequence of the thermal evolution of amorphous silicates, rather than arising from a distinct mixture of amorphous and crystalline materials.

From the foregoing arguments, it would appear that the physical changes occurring within the silicate that give rise to some of the 10 μm band fine structure do not correlate with the observed crystalline evolution as defined within the limits of the minimum X-ray resolution or the crystallite correlation length.

The feature at ~11.2 μm, initially present in the unprocessed amorphous sample as a shoulder is the first feature to develop as a peak in the 10 μm region in terms of both annealing temperature and exposure time. At the lowest annealing temperature of 873 K and 4 hours exposure it appears to develop as an obvious peak while the three 20 μm features are still somewhat broad and poorly defined. Commonly attributed to the Si-O stretch for SiO_4 species, its strength appears to grow in association with the 20 μm features as both annealing time and temperature increase. As we have identified the 20 μm features with forsteritic olivine (and in particular the 23.8 μm feature) the association of the 11.2 μm feature with forsterite appears to be confirmed along with the correlation of its strength with the formation of crystalline structure.

The development of a feature at ~9.3 μm in the data from 970 K onwards is also interesting. Although Jäger et al. (1998) identify the presence of a feature at this position in synthetic 100% Mg forsterite (which in their data disappears with increasing Fe content), the presence of a feature at 9.3 μm is more commonly attributed to crystalline pyroxene spectra (e.g. Koike et al. 1981, 1993; Jäger et al. 1998; Brucato et al. 1999b). Observations of Comet Hale-Bopp by Wooden et al. (1999) have shown the presence of a 9.3 μm feature that increases in strength as the comet approaches perihelion. The development of this feature in the comet spectra is also accompanied by the development of three weak features at 10.5, 10.8 and 11.8 μm which are also present in our data. Grains with pyroxene compositions are implied by the PUMA-1 results (Jessberger et al. 1988; Lawler et al. 1989) for Comet Halley and differences between the 10 μm bands for various comets have previously been attributed (at least in part) to variations in the relative abundance of crystalline/amorphous olivines and amorphous pyroxenes (as well as to the Mg:Fe ratio). Amorphous pyroxene grains have been invoked to explain the short-wavelength rise of the 10 μm band as well as the 9.8 μm peak, for example in Comet Halley (e.g. Hanner et al. 1994b; Colangeli et al. 1995). Despite this, and the identification of Mg-rich pyroxenes in certain types of interplanetary dust particles (Bradley et al. 1997), the presence of crystalline pyroxene has not been inferred from the 10 μm band spectra of comets prior to Hale-Bopp (Wooden et al. 1999). At 2.8 AU Wooden et al. observed the 10 μm band of Hale-Bopp to be similar to Halley's and fitted its spectra with a three component mineral mixture: amorphous olivine with 50% Mg (relative to Fe), crystalline olivine with 90% Mg and amorphous pyroxene with 100% Mg. At 1.7 AU they report the presence of a 9.3 μm peak along with the three features at 10.5, 10.8 and 11.8 μm and suggest the evolution of such features at short heliocentric distances to be due to the addition of a fourth mineral phase, obtaining a fit at 9.3 μm using crystalline pyroxene with a Mg content $\geq$ 90%. To explain the non-appearance of this extra crystalline phase at greater distances they suggest that the high Mg content of crystalline pyroxene makes its grains less optically active and therefore cooler than Mg-rich olivine grains. An alternative possibility for the 9.3 μm feature carrier could be a pure, amorphous SiO_n such as SiO_2 or Si_2O_3 which have peak absorbances near 9.2–9.3 μm. These should also be accompanied by other features such as a shoulder at ~8.4 μm and a peak at 11.4 μm for Si_2O_3 and a peak at ~12.5 μm for SiO_2. However inspection of our spectra does not reveal the presence of these additional features. As a note of caution however, we draw attention to the fact that the current literature relating to laboratory silicate analogues presents results obtained from samples manufactured by a variety of methods. Thus there is a large question concerning the parity between the various results, as well as how well the various samples adequately model real cosmic silicates. Samples produced as condensates of Mg and SiO vapours not only tend to lack many full SiO_4 tetrahedra, but will also contain free silica, MgO oxides and Mg metal. Such samples are therefore (in terms of silicate) highly disordered both structurally and chemically. Samples produced by laser ablation of mineral specimen will contain condensed, non-crystalline particles as well as liquid drops and solid spall from the target. Gel desiccation on the other hand tends to produce silicates that are chemically well defined with a well established, but disordered, tetrahedral environment. The samples produced by each of these techniques are in turn also dependent on the precise details governing the manufacturing processes involved. These differences of production can ultimately lead to a difference in physical behaviour. As noted previously (Thompson & Tang 2001), samples such as vapour condensed silicate may require substatially higher annealing temperatures in order to crystallise. However cometary grains are likely to have suffered post-formation processing in stellar atmospheres, the interstellar medium and pre-solar nebular

prior to incorporation into comet bodies and thus may not be best modelled by samples more representative of freshly nucleated dust grains. Therefore, whilst we acknowledge the method of manufacture of our initial silicate might yield a somewhat idealised analogue to comet dust, it should be borne in mind that the validity of fitting observed spectra with laboratory data obtained from fully crystalline materials does rely explicitly on the underlying assumption that such features can be definitively attributed to crystalline grain components with certain macroscopic structures. That we have found, using two complimentary techniques, that a sample of amorphous pyroxene composition can crystallise to a forsterite structure and still display certain pyroxene-like fine-structure features does at the very least open up the possibility that certain of the features seen in the 10 μm band of objects such as comets might not correlate directly with the macroscopic crystalline grain structure. After all, the features in this region are generally accepted as being independent of the material's long-range structure. In such instances, fits to pyroxene-like features in the 10 μm band would have to be constrained by the spectral behaviour at other wavelengths before necessarily being accepted as definitive. In the case of Hale-Bopp, features seen at longer wavelengths (19.5, 23.5 and 33.5 μm) at pre-perihelion distances have already been identified with forsterite (Crovisier et al. 1997). Presumably the appearance of crystalline pyroxene grains at perihelion should also be detectable at longer wavelengths.

There are several possible plausible explanations for the presence of these "crystalline" enstatite features in a crystalline forsterite dominated sample. Firstly, given the absence of enstatite features in the diffraction data, they could originate from micro-crystalline enstatite structures, too small to be detected using our current diffraction apparatus, or they could represent an ultra dilute phase whose presence would require much greater detector integration times to detect than those employed in our measurements. In both cases, this would imply a 10 μm spectral response for enstatite that is very strong in relation to its physical extent (and also relative to forsterite) and presumably a 20 μm response that is correspondingly weaker so as not to be visible in this band. IR spectroscopy only returns information regarding the average bond type. Thus, while there may be sufficient "enstatite" Si-O bonds to produce features in the 10 μm band, to produce features in the 20 μm band would require these to be arranged in an enstatite lattice, which is clearly not the case. A more realistic possibility could be that these features represent an improvement in the local SiO_3 ordering arising as a result of annealing, but without the formation of regular crystallographic structure. Such changes for example could result from wide-spread, but highly localised, changes (e.g. changes in polymerisation) that do not repeat in a regular way over macroscopic lengths, or could represent changes in the inter-linked tetrahedral environment that are not reliant on any one particular macroscopic structural arrangement being adopted. As such the appearance of these pre-crystalline enstatite features in observed spectra may only signal that the silicate has been annealed, rather than actually tell us something about the macroscopic structure of the material itself. It is therefore worth stressing that this finding could potentially offer new perspectives on the reconstruction of the thermal history of comets, even if at this stage it is deserving of more detailed study.

Previously reported XRD annealing results (Thompson & Tang 2001) show the forsterite structure formed in this $MgSiO_3$ powder persists as the prominent crystal phase at least up to 1173 K, whether further annealing at this, or higher, temperatures would eventually produce a phase change resulting in the expected enstatite pyroxene structure is currently unknown. The formation of macroscopic crystalline pyroxene structures from amorphous grains could in fact be harder to realise than their composition alone suggests.

5. Conclusions

Both the XRD data and corresponding IR spectra at 20 μm confirmed the formation of forsterite in the annealed pyroxene samples. Both sets of data also showed that crystallisation was incomplete. The evolution of the 20 μm band, even at 1000 K, tended to show more variation than the XRD data, suggesting that IR spectroscopy is perhaps more sensitive to small scale variations than can be determined from XRD, which gives a bulk snap-shot of the average sample structure, whereby small amounts of variation can be averaged out by the rest of the sample. This difference can be understood by considering the nature of the two techniques. XRD is a probe of long-range configurational correlations, whilst IR bands are sensitive to changes in the lattice dynamics of the individual SiO_n units. Although XRD is invaluable as a structural fingerprint, its apparent insensitivity relative to the 10 μm band suggests the changes revealed by IR spectroscopy in this band are not structurally correlated over long length scales and indeed may even be to some degree insensitive to the specific crystallographic silicate structure. However, even if IR spectroscopy is in some instances less indicative of the overall structural arrangement, we must bear in mind that so far this is the only astronomical tool available with which to probe the in situ changes apparent in cometary grains. We conclude therefore that in the laboratory such combined techniques are particularly useful in studying the possible processes to which grains are subjected, since experiments designed to explicitly reproduce only the astronomical data are unlikely to reveal the full picture behind grain histories as the specific parameter space explored by them is unlikely to be enough on its own to allow unique fits or constraints to be found.

In conclusion, we have presented the results of annealing experiments on an initially amorphous $MgSiO_3$ silicate system as its structure changes from amorphous to crystalline. Using the combined techniques of synchrotron X-ray powder diffraction and IR spectroscopy we have shown that this particular system can crystallise on a local scale to a forsterite (Mg_2SiO_4) structure. However, we have also identified the presence in the crystalline IR spectra of our sample certain 10 μm band features usually attributed to the presence of crystalline enstatite ($MgSiO_3$), a phase that appears to be absent from our annealed sample when viewed using XRD. This raises the possibility that, in the absence of corroborating features at other wavelengths, the detection of 10 μm band "crystalline enstatite" features in comets and other objects may not be enough to

definitively identify the presence of crystalline enstatite grains. Such features may originate in improvements to the short-range ordering of the amorphous $MgSiO_3$ grain components as a result of the grains having been annealed and does not necessarily require the formation of bulk crystalline enstatite. These findings could have potentially significant consequences for the reconstruction of the thermal history of comets along with implications for our understanding of the evolution of the solar system.

Acknowledgements. This work has been partially supported by the Italian Space Agency (ASI) and the Italian Ministry of University and Research (MIUR). The authors would also like to express their thanks to J. A. Nuth for his helpfull and constructive comments during the refereeing of this paper.

References

Bailey, M. E. 1987, QJRAS, 28, 242
Bailey, M. E. 1994, in Asteroids, comets, Meteors 1993, ed. A. Milani (Kluwer, Dordrecht), 443
Blanco, A., Fonti, S., & Orofino, V. 1999, PSS, 47, 781
Borghesi, A., Bussoletti, E., & Colangeli, L. 1985, A&A, 142, 225
Bradley, J. P., Brownlee, D. E., & Snow, T. P. 1997 in From stardust to planetesimals, ed. Y. J. Pendleton, A. G. G. M. Tielens, vol 122, BookCrfters, San Francisco, ASP Conf. Ser., 108, 217
Bregman, J. D., Campins, H., Witteborn, F. C., et al. 1987, A&A, 187, 616
Brucato, J. R., Colangeli, L., Mennella, V., Palumbo, P., & Bussoletti, E. 1999a, PSS, 47, 773
Brucato, J. R., Colangeli, L., Mennella, V., Palumbo, P., & Bussoletti, E. 1999b, A&A, 348, 1012
Bussoletti, E., Colangeli, L., Borghesi, A., & Orofino, V. 1987, A&A, Suppl. Ser., 70, 257
Campins, H., & Ryan, B. V. 1989, ApJ, 341, 1059
Cernik, R. J., Murray, P. K., Pattison, P., & Fitch, A. N. 1990, J. Appl. Cryst., 23, 292
Chick, K. M., Cassen, P. 1997, ApJ, 477, 398
Colangeli, L., Mennella, V., di Marino, C., Rotundi, A., & Bussoletti, E. 1995, A&A, 293, 927
Colangeli, L., Mennella, V., Rotundi, A., Palumbo, P., & Bussoletti, E. 1996, A&A, 312, 643
Collins, S. P., Cernik, R. J., Pattison, P., Bell, A. M. T., & Fitch, A. N. 1992, Rev. Sci. Instrum., 63, 1013
Crovisier, J., Brooke, T. Y., Hanner, M. S., et al. 1996, A&A, 315, L385
Crovisier, J., Leech, K., Bockelee-Morvan, D., et al. 1997, Science, 275, 1904
Crovisier, J., Leech, K., Bockelee-Morvan, D., et al. 1999, in The universe as seen by ISO, ed. P. Cox, & M. F. Kessler, ESA-SP, 427, 137
Day, K. L. 1974, ApJ, 234, 158
Debrenne, P., Laugier, J., & Chaudet, M. J. 1970, Appl. Cryst., 3, 493
Delsemme, A. H. 1999, PSS, 47, 125
Dorschner, J., Friedmann, C., Gurtler, J., & Henning, Th. 1988, A&A, 198, 223
Ferlet, R., Vidal-Madjar, A., & Hobbs, L. M. 1987, A&A, 185, 267
Fernandez, J. A., & Ip, W. H. 1981, Icarus, 47, 470
Fernandez, J. A., & Ip, W. H. 1983, Icarus, 54, 377
Greenberg, J. M., & Li, A. 1996, in The role of dust in the formation of stars, ed. H. U. Kaufl, & R. Siebenmorgen (Springer), 161
Hallenbeck, S. L., Nuth, J. A., & Daukantas, P. L. 1998, Icarus, 131, 198
Hanner, M. S., Hackwell, J. A., Russell, R. W., & Lynch, D. K. 1994a, Icarus, 112, 490
Hanner, M. S., Lynch, D. K., & Russell, R. W. 1994b, ApJ, 425, 274
Hart, M., & Parrish, W. 1986, Matrls Sci. Forum, 9, 3946
Hayward, T. L., & Hanner, M. S. 1997, Science, 275, 1907
Hecht, J. H., Russel, R. W., Stephens, J. R., & Grieve, P. R. 1986, ApJ, 309, 90
Heslin, M. R. 1993, Ph.D. Thesis, Alfred University
Hills, J. G. 1982, AJ, 87, 906
Hills, J. G., & Sandford, M. T. 1983, AJ, 88, 1519
Hobbs, L. M. 1986, ApJ, 308, 854
Ip, W. H., & Fernandez, J. A. 1988, Icarus, 74, 47
Jäger, C., Molster, F. J., Dorschner, J., et al. 1998, A&A, 339, 904
Jessberger, E. K. A., Christoforidis, A., & Kissel, J. 1988, Nature, 332, 691
Knacke, R. F., Fajardo-Acosta, S. B., Telesco, C. M., et al. 1993, ApJ, 418, 440
Koike, C., Hasegawa, H., Asada, N., & Hattori, T. 1981, ASS, 79, 77
Koike, C., Shibai, H., & Tuchiyama, A. 1993, MNRAS, 264, 654
Lawler, M. E., Brownlee, D. E., Temple, S., & Wheelock, M. N. 1989, Icarus, 80, 225
Morimoto, Y., Igarashi, T., Sugahara, H., & Nasu, S. 1992, J. Non-Cryst Sol., 139, 35
McMillan, P. 1984a, Amer. Miner., 69, 622
McMillan, P. 1984b, Amer. Miner., 69, 645
Munro, I. H. 1997, J. Synchrotron Rad., 4, 344
Napier, W. M., & Clube, S. V. M. 1997, Rep. Prog. Phys., 60, 293
Nuth, J. A., & Donn, B. 1982, ApJ, 257, L103
Nuth, J. A., & Hecht, J. H. 1990, ASS, 163, 79
Nuth, J. A., Hill, H. G. M., & Kletetschka, G. 2000, Nature, 406, 275
Oort, J. H. 1950, Bull. Astron. Inst. Neth., 11, 91
Parrish, W., Hart, M., Erickson, C. G., Masciocchi, N., & Huang, T. C. 1986, Adv X-ray Anal., 29, 243
Russell, R. W., & Lynch, D. K. 1996, IAU Circ., 6448
Rietmeijer, F. J. M., Nuth, J. A., & Mackinnon, I. D. R. 1986, Icarus, 66, 211
Rietmeijer, F. J. M., Hallenbeck, S. L., & Karner, J. M. 2002, Icarus, 146, 269
Sabatier, G. 1950, CR Acad Sci. Paris, 230, 1962
Safronov, V. S. 1969, NASA TT-F-677 206
Safronov, V. S. 1972, in The motion, evolution and origin of comets, ed. G. A. Chebotarev, et al. (Springer Verlag, NY), 329
Shackelford, J. F., & Masaryk, J. S. 1976, J. Non-Cryst. Sol., 21, 55
Sitko, M, Grady, C. A., Lynch, D. K., Russell, R. W., & Hanner, M. S. 1999, ApJ, 510, 408
Sitko, M, Grady, C. A., Russell, R. W., et al. 2000, in Protostars and planets IV, ed. V. Manning, A. P. Boss, & S. S. Russell (Univ. Arizona Press, Tuscon), 613
Shelby, J. E. 1977, J. Appl. Phys., 48, 3387
Shelby, J. E. 1994, J. Non-cryst. Sol., 179, 138
Steel, T. M., & Duely, W. W. 1987, ApJ, 315, 337
Stephens, J. R., Blanco, A., Bussoletti, E., et al. 1995, PSS, 43, 1241
Tang, C. C., Bushnell-Wye, G., & Cernik, R. J. 1998, J. Synchrotron Rad., 5, 929
Thompson, S. P. 1996, Astro. Lett. & Comm., 33, 299
Thompson, S. P., & Tang, C. C. 2001, A&A, 368, 721
Tielens, A. G. G. M., & Allamandola, L. J. 1990, in Interstellar Processes, ed. D. J. Hollenbach, & H. A. Thronson, Riedel, Dordrecht, 397
Timmermann, R., & Larson, H. P. 1993, ApJ, 415, 820
van der Steen, G. H. A. M. 1976, Ph.D. Thesis, University of Eindhoven
Warren, B. E. 1969, X-ray diffraction, Adisson-Wesley, Massachusetts
Weissman, P. R. 1995, A&A, Rev., 33, 327
Whittaker, E. J. W. 1981, Crystallography, Pergamon, Oxford
Wooden, D. H., Harker, D. E., Woodward, C. E., et al. 1999, ApJ, 517, 1034